Chiral-structured heterointerfaces enable durable perovskite solar cells

Tianwei Duan[1,#], Shuai You[2,#], Min Chen[2,#], Wenjian Yu[1], Yanyan Li[3,4], Peijun Guo[3,4], Joseph J. Berry[2, 6, 7], Joseph M. Luther[2], Kai Zhu[2,*], Yuanyuan Zhou[5,*]

[1] Department of Physics, Hong Kong Baptist University, Kowloon, Hong Kong SAR 999077, China

[2] Chemistry and Nanoscience Center, National Renewable Energy Laboratory, Golden, CO 80401, USA

[3] Department of Chemical and Environmental Engineering, Yale University, New Haven, CT 06520, USA

[4] Energy Sciences Institute, Yale University, West Haven, CT 06516, USA

[5] Department of Chemical and Biological Engineering, The Hong Kong University of Science and Technology, Clear Water Bay, Hong Kong SAR 999077, China

[6] Renewable and Sustainable Energy Institute, University of Colorado Boulder, Boulder, CO 80303, USA

[7] Department of Physics, University of Colorado Boulder, Boulder, CO 80302, USA

[*] Corresponding author: yyzhou@ust.hk (Y.Z.); kai.zhu@nrel.gov (K.Z.)

[#] Equal contribution

Abstract:

Mechanical failure and chemical degradation of device heterointerfaces can strongly influence the long-term stability of perovskite solar cells (PSCs) under thermal cycling and damp heat conditions. We report chirality-mediated interfaces based on *R-/S*-methylbenzyl-ammonium between the perovskite absorber and electron-transport layer to create an elastic yet strong heterointerface with increased mechanical reliability. This interface harnesses enantiomer-controlled entropy to enhance tolerance to thermal-cycling-induced fatigue and material degradation, and a heterochiral arrangement of organic cations leads to closer packing of benzene rings that enhances chemical stability and charge transfer. The encapsulated PSCs showed retentions of 92% of power conversion efficiency under the thermal cycling test (−40ºC to 85ºC; 200 cycles over 1200 h) and 92% under a damp heat test (85% relative humidity (RH); 85ºC; 600 h).

One-Sentence Summary: High-density molecular packing using an equal amount of chiral *R*- and *S*-methylbenzyl-ammonium strengthens the interface between electron transporting contacts and halide perovskite light absorbers, enhancing both the mechanical reliability and chemical stability of perovskite solar cells with improved power-conversion efficiency and device operation stability under thermal cycling and damp heat conditions.

Main Text:

Perovskite solar cells (PSCs) have been demonstrated as a highly cost-effective photovoltaic technology with impressive performance (*1*–*7*). Organic-inorganic halide perovskites (OIHPs), the essential light absorbers in PSCs, have exceptional photophysical properties and compatibility with established commercial manufacturing processes (*8*), and certified power-conversion efficiencies (PCEs) of single-junction PSCs as high as 26.1% have been reported (*9*). However, an important challenge faced by PSCs for withstanding real-world conditions subject to temperature variations is the relatively low mechanical reliability of their critical interfaces, especially those where the two sides have different coefficients of thermal expansion (*10*, *11*). For example, temperature variations associated with diurnal cycles—along with the coefficient of thermal expansion mismatch between different device layers—can lead to interfacial sliding, interlayer delamination, and void formation, ultimately resulting in mechanical failure and material degradation in PSCs (*12*).

Despite the importance of this problem, there are a limited number of reported efforts specifically targeting interface failures in PSCs (*10*, *13*, *14*). Reported strategies to mitigate thermal-cycling fatigue include exploring thermally stable materials (*5*, *12*, *15*–*17*), alleviating interfacial stress (*18*), and refining encapsulation methods (*19*). Although these strategies help improve the thermal stability of materials, more efforts are needed to address the critical challenges related to mechanical reliability at the heterointerfaces. Functional head and tail groups of any incorporated interfacial layer need to be designed that strengthen the bonding between the charge-transport layer and the OIHP surface and also maintain the carrier transport. Conventionally, in tackling interfacial problems, interface passivation has been used to strengthen the interaction between the charge-transport layer and the OIHP (*20*–*22*). Organic molecules at the interface can also serve as a barrier against environmental factors to improve chemical stability. However, the impact of interface passivation on the mechanical stability of PSCs remains unclear.

Chiral materials have intriguing optical and electronic properties (*23*), but most studies of chiral perovskite materials have focused on applications in optoelectronics and spintronics (*23–26*). Chiral structures in natural, mechanically stable biostructures adopt the form of spiral or helical microstructures and exhibit outstanding deformation tolerance and dynamic adaptability. Examples include helical DNA (*27*) and viruses (*28*), gyroid structures in butterfly wings (*29*), the cholesteric liquid crystal phase in beetle exoskeletons (*30*), and eye-distinguishable spiral aloe and seashells (*31*). Scientists have also designed artificially chiral archetypal metamaterials with distinctive mechanical properties, such as negative Poisson ratios, as well as an enhanced indentation resistance, fracture toughness, shear modulus, and dynamic energy absorption (*32–35*). The prominent mechanical properties of chiral materials are associated with the helical packing of their subunits. The packing arrangement resembles a mechanical spring, which can deflect or deform under force and restore its original shape when the force is released (*36*). However, the mechanical characteristics of chiral materials have been rarely considered for PSC development.

In this work, we leverage the high tunability of OIHPs to facilitate chiral ammonium coordination and thereby introduce a chiral perovskite interlayer. This chiral interlayer enhances both the mechanical, chemical and optoelectronic properties of the electron-transport layer (ETL)/OIHP heterointerface in PSCs. In particular, we verified the improved durability of the ETL/OIHP interface with the chiral interlayer and resultant PSCs using the standardized International Electrotechnical Commission (IEC) 61215:2016 MQT 11 & 13 protocols and the American Society for Testing and Materials (ASTM) D3359 adhesion test.

Controlling the enantiomer components in the chiral microstructure can further enhance the mechanical properties, as exemplified by the stronger interface adhesion of racemic hetero-chiral perovskite interface (CPI) compared to homo-CPI. The racemic interface also has more favorable chemical stability and optoelectronic properties because it has a denser packing of hydrophobic benzene rings with their π–π stacking. We show that using a chiral perovskite interlayer improves device stability under standard thermal cycling, damp heat, and continuous light-soaking conditions that result from the improved mechanical, chemical and optoelectronic characteristics. The champion PCE of a device with a composition of $(FAPbI_3)_{0.95}(MAPbBr_3)_{0.05}$

and 0.06-cm^2 illuminated areas based on a heterochiral interlayer reached 24.3% for n-i-p PSCs and 26.0% for p-i-n PSCs. This study serves as a proof of concept, showcasing the use of chiral chemo-mechanics to further enhance the durability of optoelectronics with layered stacks.

Chiral perovskite interface formation

We chemically modulated the mechanical properties of chiral perovskite interlayers by using (i) a homochiral interface based solely on *R*-methylbenzyl-ammonium iodide (*R*-MBAI) or *S*-methylbenzyl-ammonium iodide (*S*-MBAI) and (ii) a heterochiral interface based on an equal mixture of *R*-MBAI and *S*-MBAI (*R/S*-MBAI). To form chiral-structured perovskite-substrate interlayers for conventional n-i-p structured PSCs, we deliberately incorporated chiral ammonium iodide (*R*- or *S*-MBAI) into the SnO_2 ETL, paired with excess PbI_2 in the perovskite absorber layer. For inverted p-i-n structured PSCs, we spin-coated *R*- or *S*-MBAI in an isopropanol solution atop the perovskite layer. This step was followed by an annealing-induced interdiffusion reaction that creates a chiral perovskite interfacial layer between the ETL and the perovskite layers that generates a rotational axis in the crystalline phase in the interlayer **(Fig. 1A**).

Ideally, this chiral interlayer should consider the following design criteria. First, the chiral molecules should form a homogeneous interface with the adjacent layers to ensure processing reproducibility. Second, the chiral molecules should contain functional groups that can produce *van der Waals* forces to enable adaptable binding at the interlayer. Third, the chiral interlayer should mitigate interfacial defects to facilitate charge transfer with minimized recombination. Following these considerations, we chose a pair of enantiomers, *R*- and *S*-MBAI, for developing chiral perovskite interlayers.

Taking the interlayer modulation for enhancing n-i-p PSCs' mechanical properties as an example, as schematically illustrated in **Fig. 1A**, the 2D homochiral and heterochiral perovskite interfaces—(R-MBA)$_2$PbI$_4$ and (R/S-MBA)$_2$PbI$_4$—form from a reaction of the excess 4% PbI_2 in the OIHP with the *R*-MBAI or *R/S*-MBAI on the ETL, respectively. Here, (R-MBA)$_2$PbI$_4$ was chosen as a typical case of a homochiral perovskite; its enantiomer compound, (S-MBA)$_2$PbI$_4$, shared an opposing configuration. We first confirmed the formation of chiral molecule enantiomers by observing the mirrored circular dichroism signals in *R*-MBAI and *S*-MBAI (centered around 257 nm), along with the silent circular dichroism signals of *R/S*-MBAI with the equivalent amount of *R*-MBAI and *S*-MBAI (Fig. S1).

Next, we performed an X-ray diffraction (XRD) measurement on the flipped, delaminated OIHP film, which exposed the bottom surface. For both the homo- and hetero-CPI in n-i-p structured films, we observed the characteristic (002) diffraction peak at $2\theta = 6.10^{\circ}$, which should be assigned to the as-formed 2D chiral perovskite phase (Fig. S2). This peak becomes more evident when elevating the concentration of buried chiral molecules. The OIHP bottom surface maintained similar microstructures after homo- or hetero-CPI formation and showed similar morphology to that of the pristine film (Fig. S3 and S4). These results suggest that thin CPI layers form through our fabrication route. Note that the 2D chiral perovskite layer was also observed in the surface passivation of a 3D perovskite in the p-i-n structure (glass/FTO/HTL/OIHPs/chiral molecule treatment/ETL). The homo-CPI and hetero-CPI formed on top of the 3D perovskite both showed the characteristic (002) diffraction peak of the 2D perovskite (Fig. S5) (*37*).

The proposed structures of the homo-CPIs are given by the corresponding single-crystal structures of $(R\text{-MBA})_2PbI_4$ and $(S\text{-MBA})_2PbI_4$ (Fig. S6) (*38*). Although there are various possible heterochiral molecule packings in an enantiomer mixture like $(R/S\text{-MBA})_2PbI_4$, the difference in binding energy among these isomers would be quite small (Fig. S7). Thus, we used a single-crystal $(R/S\text{-MBA})_2PbI_4$ structure (*39*)—the most stable structure—for the hetero-CPI in the following context to study the chemical and mechanical properties. As shown in **Fig. 1B,** the as-formed 2D chiral perovskite can be conceptualized as a combination of inorganic sheets of PbI_4^{2-} and bilayers of MBA^+ molecules. The inorganic sheets consist of corner-sharing metal-halide octahedra. The monovalent MBA^+ molecules form bilayers between these inorganic sheets, which are linked by the hydrogen bonds between the ammonium head of the MBA^+ and the I^- ions in the axial position of the octahedra. Two MBA^+ cations fill in the space above and below each octahedron that shares four corners in the *ab* crystal plane.

Because the amine enantiomers have distinct spatial configurations, the organic bilayers in homochiral and heterochiral perovskites were laid out differently between the inorganic sheet layers. In the homochiral perovskite $(R\text{-MBA})_2PbI_4$ with the $P2_12_12_1$ space group, the arrangement of the two $R\text{-MBA}^+$ bilayers between inorganic sheets are rotational along the *a*-, *b*-, and *c*-axis, resulting in helical stacking with the 2_1 helical axis in three directions. In contrast, because of the geometry difference of the enantiomer, the heterochiral bilayers of $R\text{-MBA}^+$ and $S\text{-MBA}^+$ in $(R/S\text{-MBA})_2PbI_4$ with $P2_1/a$ space group are only rotationally arranged along the *b*-axis, with the 2_1

rotation symmetry along this axis. Meanwhile, in the *b*-axis direction of the chiral perovskite, (*R*-MBA)$_2$PbI$_4$ only has helix packing generated by right-handed molecules (red color helical strips in Fig 1B), whereas (*R/S*-MBA)$_2$PbI$_4$ has both left- and right-handed molecule helical packing (blue and red color helical strips in Fig 1B). These two helical packing strips are bonded by π–π stacking of the benzene rings from the same and opposing configurations for (*R*-MBA)$_2$PbI$_4$ and (*R/S*-MBA)$_2$PbI$_4$, respectively.

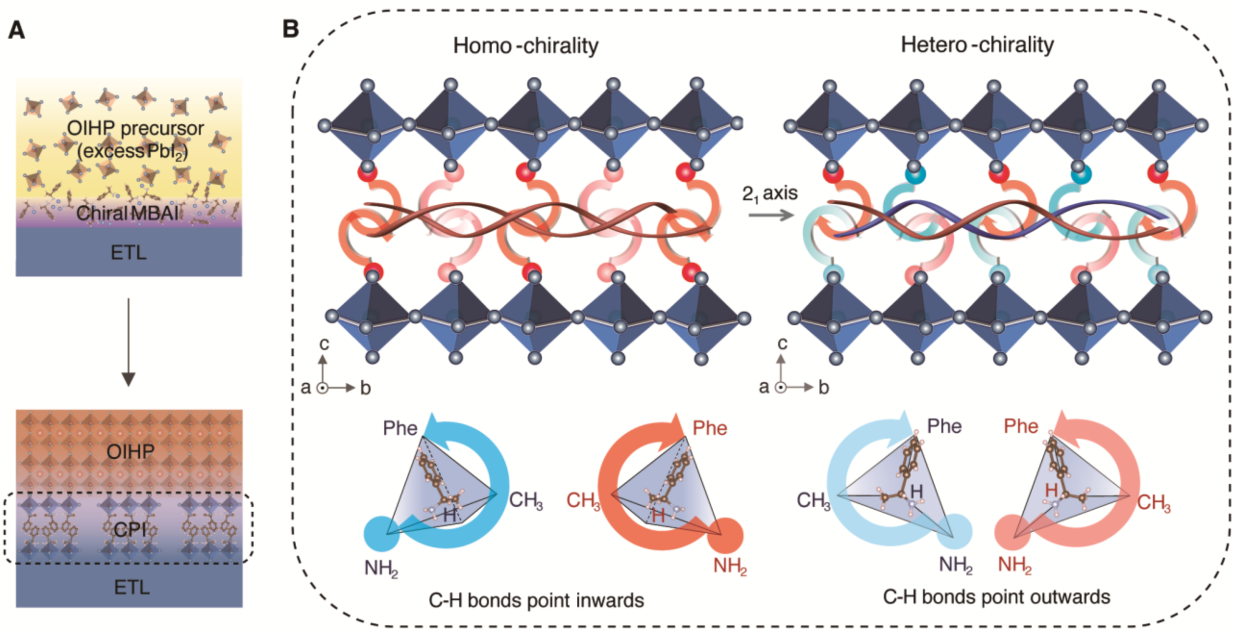

Fig. 1. Schematic of homochiral and heterochiral interface modification. (A) The homochiral perovskite (*R*-MBA)$_2$PbI$_4$ and heterochiral perovskite (*R/S*-MBA)$_2$PbI$_4$ are formed by the reaction of the *R*-MBAI or *R/S*-MBAI (1:1 molar ratio of *R*-MBA$^+$ to *S*-MBA$^+$) with excess PbI$_2$ at the interface of OIHP with ETL. The octahedra for the CPI and 3D OIHP are illustrated in blue and brown, respectively. (B) The stacking pattern of the two adjacent organic bilayers is non-colinear in (*R*-MBA)$_2$PbI$_4$ and colinear in (*R/S*-MBA)$_2$PbI$_4$, viewed along the *a*-axis. In the *b*-axis direction, (*R*-MBA)$_2$PbI$_4$ and (*R/S*-MBA)$_2$PbI$_4$ have a 2_1 rotational axis containing two benzene rings with π–π stacking of homochiral and heterochiral organic ammonium, respectively. The simple models of *R*-MBA in red and light red represent C-H bonds that point straight inward or outward, respectively. The simple models of *S*-MBA in blue and light blue represent C-H bonds that point straight inward or outward, respectively.

Interfacial mechanical properties

We studied the mechanical properties of the chiral-structured interlayer based on the SnO_2/OIHP interface that is typically adopted for n-i-p structured PSCs. The delamination resistance of OIHPs was evaluated according to the film adhesion test. As depicted in **Fig. 2A**, the samples for mechanical tests were prepared as symmetrical sandwich structures. First, a thin layer of polymethyl methacrylate was spin-coated on OIHPs to protect the perovskite from chemical corrosion and surface strain from the epoxy glue. Next, a multi-blade tool with seven edges spaced 1 mm apart was used to crosscut the OIHP coating and penetrate the substrate. An epoxy resin was coated on the carved OIHP and covered by a piece of indium tin oxide (ITO) glass on the sample, which was placed in a glove box at room temperature for more than 24 hours to cure the polymer. Finally, the top-covered ITO was peeled off to leave the strongly adhered part of the OIHP on the substrate. Generally, we observed that OIHPs with homo- and hetero-CPIs have more intact areas (squares, as illustrated in Fig. 2A) than pristine structures. We also assessed the mechanical reliability of homo- and hetero-CPI in comparison to a nonchiral OIHP/ETL interface created using phenethylammonium iodide (PEAI), a prevalent achiral interface passivation molecule and an isomer of MBAI ($C_8H_{12}IN$). Although the PEAI-based interlayer also improved the adhesion between OIHP and ETL, it was not as effective as the homo- and hetero-CPIs.

To acquire the statistical evidence for the enhanced mechanical reliability of these interfaces, we assessed the 20 crosscut areas of OIHPs for each of the four samples (pristine SnO_2, homo-CPI, hetero-CPI, and PEAI) through ASTM D3359 adhesion classification (Fig. 2B, and Fig. S8). The adhesion-delamination classification was determined by the retained parts of the crosscut area, which displayed enhanced adhesion from 0B to 5B in accordance with the standard (Table S1). Specifically, the OIHP adhesion on pristine SnO_2 was classified as 2B, corresponding to an area > 15% but < 35% of the area affected across the grid, whereas the homo-CPI and hetero-CPI cases were classified as 3B, corresponding to > 5% but < 15% of the area affected across the grid. Compared with homo-CPI, OIHPs with hetero-CPI had an overall higher degree of adhesion. Moreover, only homo- and hetero-CPI samples exhibited 5B grade adhesion results, accounting for 5% and 15% of the respective samples, corresponding to none of the squares affected. OIHPs adhesion on the control PEAI-modified interface is classified between 2B and 3B, indicating relatively less significant improvement. These results underscored the value of using chiral geometry to improve mechanical adhesion.

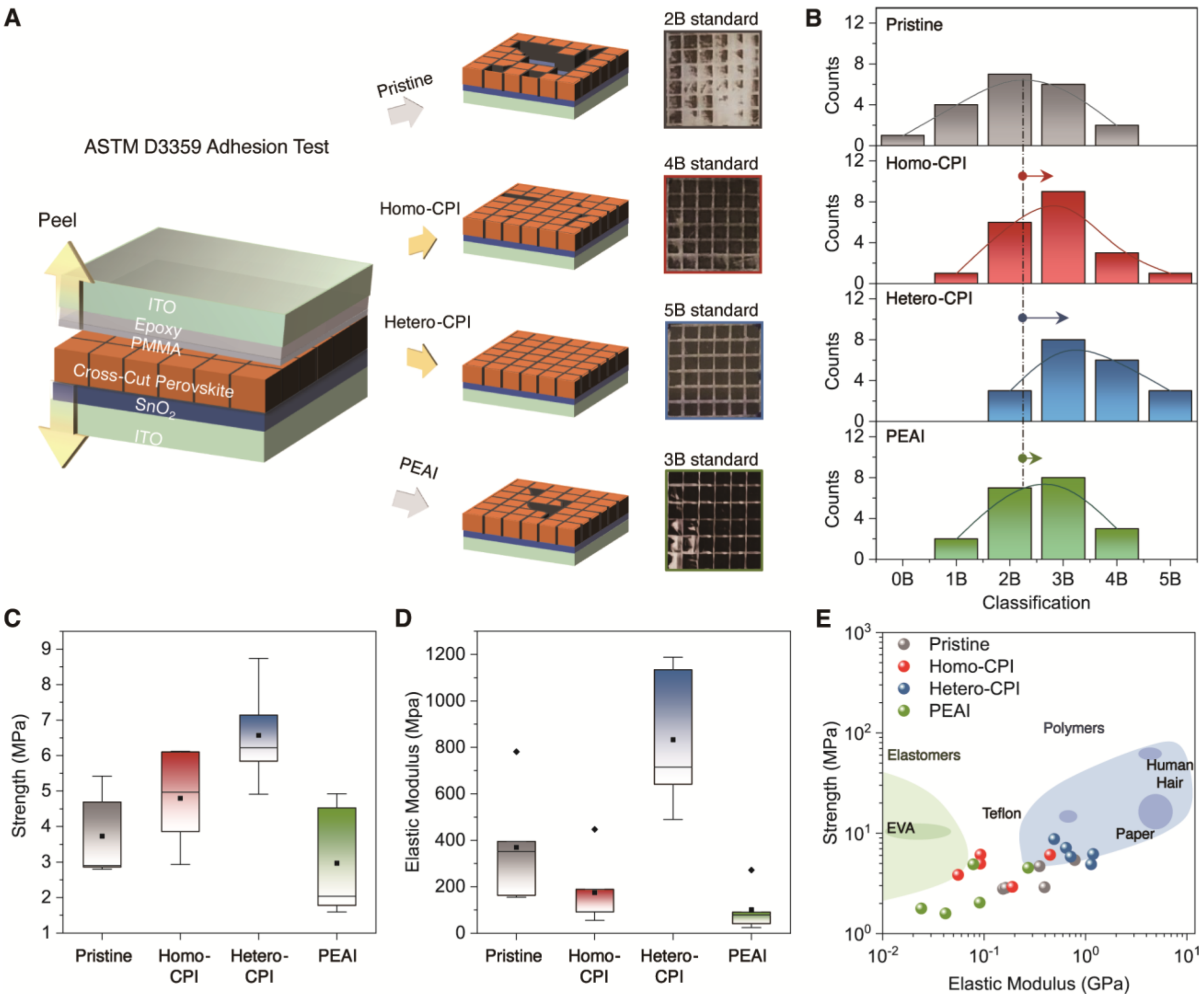

Fig. 2. Mechanical properties of the ETL/OIHP interface. (A) Schematic of the adhesion test and adhesion classification statistics for the perovskite layers on pristine SnO_2, homo-CPI, and hetero-CPI, respectively. A polymethyl methacrylate (PMMA) layer was placed on top of the perovskite layer to prevent epoxy corrosion. A crosscut pattern penetrating through the perovskite to the substrate was made to evaluate the intact part after peeling off the top ITO glass. (B) Classification of adhesion-delamination results for the perovskite layers on pristine SnO_2, homo-CPI, and hetero-CPI, PEAI interface, respectively. There are 20 crosscut sections for each film type. The evaluation was based on the ASTM D3359 standard. (C) Fracture strength statistics for

perovskites on pristine SnO_2, homo-CPI, hetero-CPI, and PEAI interface, respectively. (D) Young's modulus statistics for perovskites on pristine SnO_2, homo-CPI, hetero-CPI, and PEAI interface, respectively. The black square is the mean value of the data, and the black diamond is the outlier of the data. (E) Elastic modulus-strength map for perovskites on pristine SnO_2, homo-CPI, hetero-CPI, and PEAI interface, compared to elastomers and polymers. Each material type consists of five samples for the fracture strength and Young's modulus statistics. Data of elastomers and polymers reproduced from ref. 40, AAAS, copyright 2019.

We further studied the mechanical properties of the ETL/OIHP interface using uniaxial tensile testing (*12*). The specimen's structure was similar to that used for the adhesion tests, except for a generated tiny notch by blade at the ETL/OIHP interface to guide the fracture at the interface. The strain-stress curves show that the strength (maximum detachment stress) of pristine ETL/OIHP ($\sigma_{Pristine}$ = 4.70 MPa) is smaller than that for the homo-CPI ($\sigma_{Homo\text{-}CPI}$ = 6.12 MPa) and hetero-CPI ($\sigma_{Hetero\text{-}CPI}$ = 8.76 MPa) cases, but comparable to the PEAI-modified interface (σ_{PEAI} = 5.17 MPa) (Fig. S9). This result is consistent with the results in Fig. 2B from the alternative delamination test. Based on the experiments, the hetero-CPI exhibits the highest elastic modulus (Young's modulus, $E_{Hetero\text{-}CPI}$ = 1182 MPa), followed by pristine SnO_2 ($E_{Pristine}$ = 352 MPa), homo-CPI ($E_{Homo\text{-}CPI}$ = 92 MPa), and PEAI (E_{PEAI} = 85 MPa). These results are derived from the linear slopes of the elastic deformation region. The hetero-CPI and pristine interfaces undergo elastic deformation throughout the tensile process, whereas irreversible plastic deformation, corresponding to the start of the nonlinear response region after the applied strain, is seen for both the homo-CPI and PEAI interfaces.

To obtain a more comprehensive understanding of the interfacial mechanical properties of these three materials, we investigated five samples of each for interfacial fracture strength and elastic modulus. The mean strength of the pristine ETL/OIHP interface was enhanced by 28% and 76% for the homo-CPI and hetero-CPI, respectively, but that was reduced by 20% for the PEAI interface (**Fig. 2C**). The mechanical strength of the interface was enhanced through the formation of (R-MBA)$_2$PbI$_4$ and (R/S-MBA)$_2$PbI$_4$ 2D perovskite. The elastic modulus decreased by 53% and 71% for the homo-CPI and PEAI interfaces, respectively, but increased by 125% for hetero-CPI (**Fig. 2D**). Here, we consider that homo-CPI acts like a molecular spring, enhancing interface elasticity, but it is more susceptible to elastic deformation, resulting in a smaller Young's modulus. In contrast, hetero-CPI, formed by connecting enantiomers with opposite chirality through π bonds, exhibits an improved Young's modulus while maintaining excellent elastic deformation recovery capability. Consequently, hetero-CPI reduces the elastic deformation displacement under the same stress compared to homo-CPI.

We attributed the large discrepancy in the elastic modulus among the three interlayers to the packing difference of organic ammonium in 2D perovskite. In the elastic modulus-strength map (**Fig. 2E**), the mechanical property of the homo-CPI was analogous to an elastomer, whereas hetero-CPI was more like a polymer (*40*). These results also implied that the racemic hetero-CPI had the highest strength and elastic modulus, as well as optimum mechanical properties. For analogy, among natural polymers, chiral polymers also demonstrate excellent strength and Young's modulus, as seen in materials like cellulose-based paper and keratin-based hair (*41*, *42*).

We also investigated the influence of the homo- and hetero-CPIs on the various mechanical properties. (R-MBA)$_2$PbI$_4$ and (R/S-MBA)$_2$PbI$_4$ theoretically exhibited distinct elastic constants (Table S2). As mentioned above, the (001) plane is the preferred growth plane for (R-MBA)$_2$PbI$_4$ and (R/S-MBA)$_2$PbI$_4$. For the layered (R-MBA)$_2$PbI$_4$ and (R/S-MBA)$_2$PbI$_4$, the strong in-plane interaction induces large in-plane elastic constants (C_{11} and C_{22}) and small C_{33} that results from the weak interlayer interaction (*43*). Because the (R-MBA)$_2$PbI$_4$ and (R/S-MBA)$_2$PbI$_4$ layers are relatively thin compared to the SnO_2 and perovskite layers, we only analysed the elastic constants based on the dominating contact crystal plane. (R/S-MBA)$_2$PbI$_4$ shows more favourable in-plane mechanical properties than (R-MBA)$_2$PbI$_4$ in that it had larger C_{11} and C_{22} values. Moreover, the larger elastic constant C_{55} of (R/S-MBA)$_2$PbI$_4$ indicates stronger resistance to shear force along the *c*-axis on the *a*-plane. Thus, incorporating a thin (R/S-MBA)$_2$PbI$_4$ layer as an interlayer leads to a higher elastic modulus.

Photoluminescence studies

We used photoluminescence (PL) and time-resolved photoluminescence (TRPL) to investigate the impact of different MBA$^+$ stacking patterns (**Fig. 3A**) on charge carrier dynamics across the ETL/OIHP interface. We first studied the intrinsic PL properties of the perovskite layers. The samples were prepared by delaminating them from the substrates as for the adhesion tests. The PL and TRPL spectra in **Fig. 3B** and **C** were obtained by 375 nm laser excitation from the air side. The fitted biexponential decay lifetimes for an OIHP film with different interfaces are shown in **Tables S3.** We found that the PL intensities for hetero- and homo-CPI cases increase by 317% and 149%, respectively, compared to that for the pristine case (**Fig. 3B**). The enhancements of the PL intensity for homo-CPI and hetero-CPI are consistent with the passivation of traps, which can reduce the nonradiative recombination from the Shockley-Read-Hall process (*44*). We measured TRPL with a pulse fluence of approximately 14.15 μJ/cm^2. The passivation at the OIHP/ETL interface by the CPIs contributes to long PL lifetimes—30.8 ns for homo-CPI and 42.9 ns for hetero-CPI, compared to 22.9 ns for pristine (**Fig. 3C**).

The PL and TRPL spectra in **Fig. 3D** and **E** were obtained by 375 nm laser excitation from the glass side around the ETL/OIHP interface. **Table S4** shows the fitted biexponential decay lifetimes for an OIHP film with different interfaces are shown. The PL spectra in **Fig. 3D** also demonstrate enhanced radiative emission of the photogenerated free carriers for the CPI-incorporated SnO_2/OIHP, likely from the formation of ultrathin 2D perovskite. This 2D motif has been shown to be effective at controlling defects at the OIHP interface. Compared to pristine SnO_2/OIHP, homo- and hetero-CPIs exhibit steady-state PL intensity increases of 228% and 170%, respectively. In addition, the PL peak position shows a slight blue shift from 808.5 nm for the pristine sample to 807.6 nm and 807.9 nm for the homo-CPI and hetero-CPI samples, respectively, which could be attributed to chiral MBAI passivating the shallow trap states near the bottom surface (*45*).

In general, the fast component of decay lifetime (τ_1) is assigned to monomolecular charge trapping into nonradiative trap states, and the slow component (τ_2) is assigned to bimolecular recombination (*46*, *47*). As shown in **Fig. 3E**, the decay lifetime of this fast compound among films is 5.49, 11.52, and 10.61 ns for pristine SnO_2, homo-CPI, and hetero-CPI, respectively. These results indicate that the density of nonradiative trap states is the highest in the pristine SnO_2/OIHP film and relatively lower in homo- and hetero-CPI/OIHP films, consistent with the steady-state spectroscopic data discussed above. Furthermore, we assessed the carrier transport dynamic of ETL/CPI on the surface of OIHP (**Fig. S10**). The inclusion of C_{60} ETL at the top OIHP results in the acceleration of fast component PL decays with 0.90, 1.26, and 0.49 ns for the pristine OIHP surface, homo-CPI, and hetero-CPI, respectively, indicating charge transfer to these CTLs (**Fig. S10** and **Table S5**). For the hetero-CPI, even greater facilitated carrier injection is seen, for which we attributed to the closer packing of benzene rings compared to that in the homo-CPI (*48*, *49*).

To further examine the effect of a chiral ETL/OIHP interface on the trap density of OIHP films, we fabricated capacitor-like devices sandwiching the OIHP films between ITO/SnO_2 and PCBM/Ag and studied them using space-charge-limited current measurements at varying biases (**Fig. 3F**). The estimated electron trap densities for OIHP films on homo-CPI and hetero-CPI decreased by 17% and 25%, respectively, in comparison to the pristine case. The decreased trap densities in the OIHP film with the chiral-structured interfaces are attributed to the passivation of interfacial defects for effective electron transport.

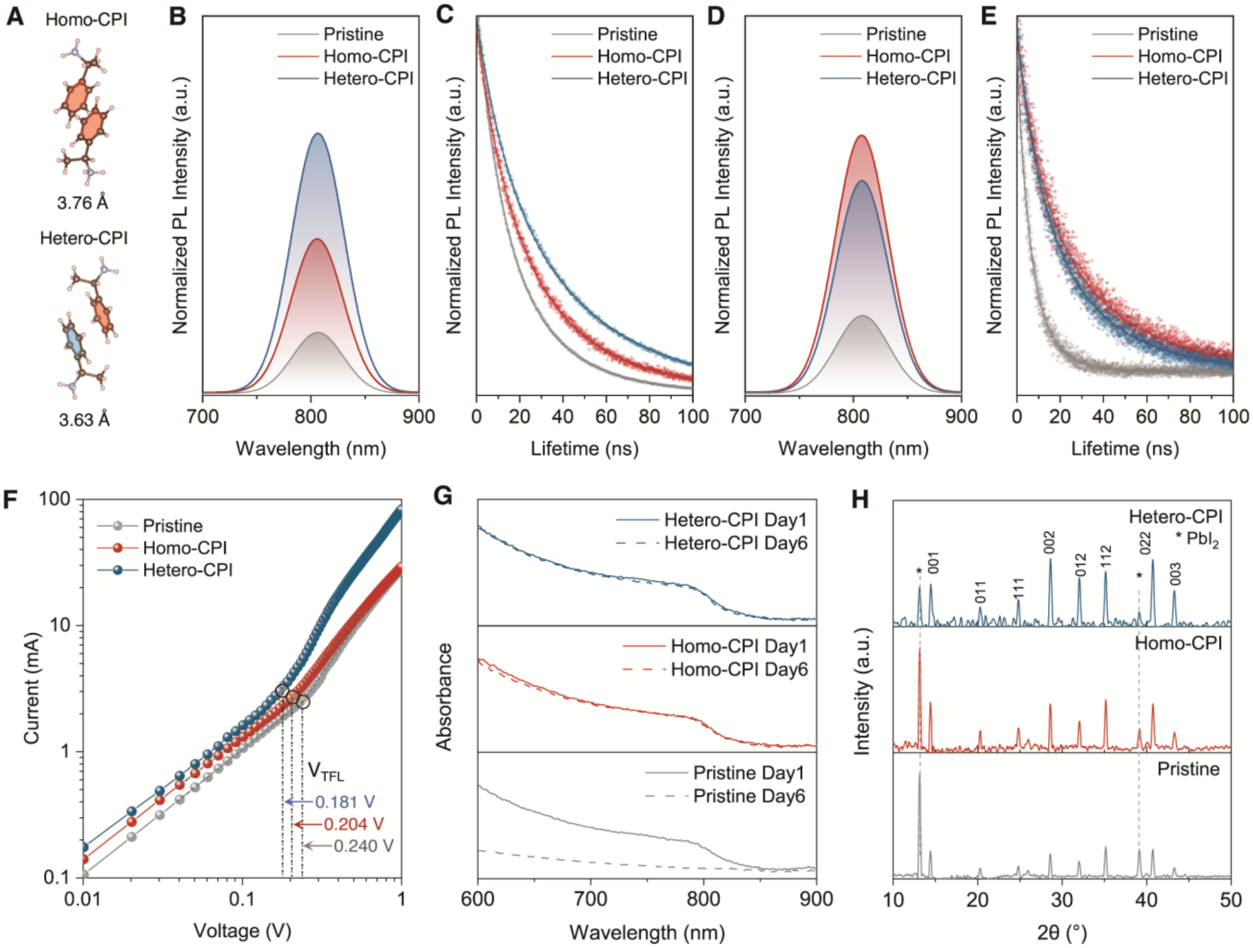

Fig. 3. Electronic properties and chemical stability of the ETL/OIHP interface. (A) The molecule packing models show π-π stacking distance of two *R*-MBA^+ molecules (3.76 Å), and *R*-MBA^+ and *S*-MBA^+ (3.63 Å), for homo-CPI and hetero-CPI, respectively. (B) PL and (C) TRPL of the flipped, delaminated OIHP film exposing the bottom surface on pristine SnO_2, homo-CPI and hetero-CPI. (D) PL and (E) TRPL of the SnO_2/OIHP interface for pristine ETL, homo-CPI,

and hetero-CPI from the glass side. (F) The space charge limit current versus voltage of devices on the OIHP/pristine SnO_2 interface, OIHP/*R*-MBAI-SnO_2, and OIHP/*R*/*S*-MBAI-SnO_2. (G) Absorption spectra of OIHP thin films stored in the ambient environment (25°C, 65% RH) on pristine SnO_2, homo-CPI, and hetero-CPI. (H) XRD patterns of the flipped, delaminated OIHP film exposing the bottom surface stored for 3 days in the ambient environment (25°C, 65% RH) on pristine SnO_2, homo-CPI, and hetero-CPI.

Chemical stability

As shown in **Fig. 3G**, the chemical stability of the three ETL/OIHPs was assessed by tracking the evolution of the ultraviolet-visible (UV-vis) absorption while the devices were stored under ambient conditions (room temperature and 65% RH). The absorption of the OIHP thin film on pristine SnO_2 decreases rapidly, and the film completely degrades in 6 days under 65% RH. The initial absorption is nearly unchanged for the OIHPs on homo- and hetero-CPIs. The degradation of the OIHP to PbI_2 is revealed by XRD for the buried interfaces, prepared through the adhesion test (**Fig. 3H**). Based on the change in the diffraction peak integrated intensity ratio—(001) for PbI_2 to (001) for OIHP—we observed that degradation is substantially slower in the homo-CPI ($I_{PbI2/OIHP}$ ~ 2.04) and hetero-CPI ($I_{PbI2/OIHP}$ ~ 0.88) samples compared to the pristine SnO_2 case ($I_{PbI2/OIHP}$ ~ 3.60). Similarly, the thermal tolerance of OIHPs on various ETLs was evaluated under the ambient heating process (100°C and 20% RH). The absorption of OIHP thin film on pristine SnO_2 decreases rapidly within 3 days in a dry box with 20% RH, compared to perovskite on a chiral additive ETL (Fig. S11).

Solar cell fabrication and testing

We fabricated PSC devices based on both n-i-p and p-i-n structures to assess the photovoltaic performance. **Fig. 4A** shows the current density–voltage (*J*-*V*) curves of n-i-p PSC devices based on pristine SnO_2, homo-CPI, and hetero-CPI at reverse scans under stimulated air mass1.5-G one-sun illumination for an active area of 0.06 cm^2. The heterochiral interlayer engineering enhances the efficiency of the devices, as seen by a champion PCE of 24.3%, a short-circuit current density (J_{SC}) of 25.0 mA cm^{-2}, an open-circuit voltage (V_{OC}) of 1.19 V, and a fill factor (*FF*) of 0.817. In comparison, the PSCs with pristine SnO_2 and homo-CPI exhibit a PCE of

21.9% and 23.7%, a V_{OC} of 1.13 V and 1.17 V, an FF of 0.791 and 0.813, and a J_{SC} of 24.5 mA cm^2 and 24.9 mA cm^2, respectively.

As shown in Fig. S12, the stabilizing power outputs (SPO) of the devices were monitored at the maximum power point for 100 s. Stabilized PCE values for devices with pristine SnO_2 and homo- and hetero-CPI were 21.2%, 23.2%, and 24.0%, respectively. **Fig. 4B** shows the *J*-*V* curves of p-i-n PSC devices based on the CPI between the HTL and OIHP. In reverse scans, the hetero-CPI engineering yields a champion PCE of 26.0%, a J_{SC} of 25.9 mA cm^{-2}, a V_{OC} of 1.18 V, and an *FF* of 85.4%. P-i-n PSCs with pristine SnO_2 and homo-CPI show a PCE of 24.0% and 25.4%, a V_{OC} of 1.14 V and 1.17 V, an *FF* of 83.5% and 85.3%, and a J_{SC} of 25.3 mA cm^2 and 25.5 mA cm^2, respectively. The SPO of the p-i-n devices with pristine SnO_2 and homo- and hetero-CPI are 23.8%, 25.1%, and 25.8%, respectively (Fig. S13). Fig. S14 shows the p-i-n devices' parameters statistics including V_{OC}, J_{SC}, *FF*, and PCE, of 15 individual PSCs based on pristine, homo-CPI and hetero-CPI, indicating good device reproducibility.

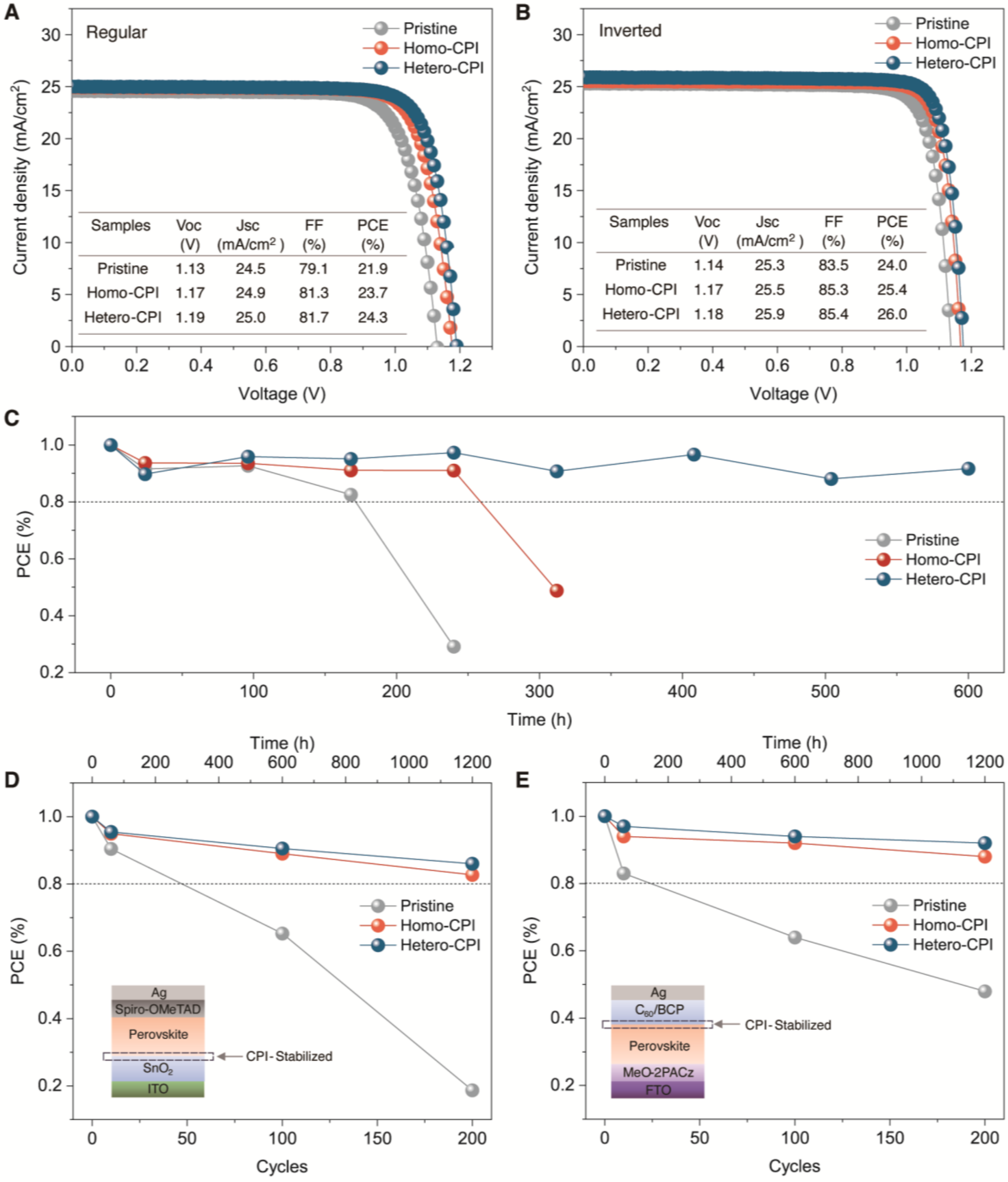

Regular

Samples	Voc (V)	Jsc (mA/cm^2)	FF (%)	PCE (%)
Pristine	1.13	24.5	79.1	21.9
Homo-CPI	1.17	24.9	81.3	23.7
Hetero-CPI	1.19	25.0	81.7	24.3

Inverted

Samples	Voc (V)	Jsc (mA/cm^2)	FF (%)	PCE (%)
Pristine	1.14	25.3	83.5	24.0
Homo-CPI	1.17	25.5	85.3	25.4
Hetero-CPI	1.18	25.9	85.4	26.0

Fig. 4. Device performance and stability of PSCs based on pristine SnO_2, homo-CPI, and hetero-CPI. (A) *J-V* curves of n-i-p PSCs based on pristine SnO_2, homo-CPI, and hetero-CPI. (B) *J-V* curves of p-i-n PSCs based on pristine SnO_2, homo-CPI, and hetero-CPI. (C) Normalized PCE of encapsulated PSCs based on pristine SnO_2, homo-CPI, and hetero-CPI under 85% RH and 85°C.

Initial PCEs for PSCs based on pristine SnO_2, homo-CPI, and hetero-CPI were 21.2%, 23.4%, and 24.1%, respectively. (D) Normalized PCE of n-i-p encapsulated PSCs based on pristine SnO_2, homo-CPI, and hetero-CPI during a temperature cycle test from −40ºC to 85ºC. Initial PCEs for PSCs based on pristine SnO_2, homo-CPI, and hetero-CPI were 21.7%, 23.6%, and 24.1%, respectively. (E) Normalized PCE of p-i-n encapsulated PSCs based on pristine SnO_2, homo-CPI, and hetero-CPI during temperature cycle tests from −40ºC to 85ºC. Initial PCEs for PSCs based on pristine SnO_2, homo-CPI, and hetero-CPI were 23.8%, 25.3%, and 25.8%, respectively.

Stability testing

The *R/S*-MBAI-engineered PSCs exhibited enhanced stability under a variety of test conditions. We initially monitored the PCE evolution under light-soaking, with the light intensity equivalent to 1 Sun (100 mW cm^{-2}). After 1360 hours, the unencapsulated PSC with hetero-CPI retains 84% PCE, indicating light stability enhancement (Fig. S15). Hetero-CPI also exhibits excellent antifatigue properties under damp heat conditions, according to the IEC 61215:2016 test standard, MQT 13 (**Fig. 4C**). The PSCs are all encapsulated using UV-curing adhesive with a cover glass. Then, the edge of the cover glass was further protected by epoxy and cured at room temperature for more than 48 hours. The glass-encapsulated device maintains 92% of its original performance after being exposed to an 85% humid environment at 85°C for 600 hours.

We also studied the thermal cycling test conditions between −40°C and 85°C using the IEC 61215:2016 MQT 11 protocol. In the conditions of thermal cycling, n-i-p PSCs based on homo- and hetero-CPIs, both preserve > 80% of their original performance after 200 cycles. However, the PCE of the pristine ETL drops rapidly to 61% after 100 temperature cycles (**Fig. 4D**). Homo- and hetero-CPIs in p-i-n PSCs manifest better retention of PCE, retaining > 88% after 200 cycles. For comparison, the PCE of the PSC with a pristine ETL drops rapidly to 64% after 100 temperature cycles (**Fig. 4E**).

In both PSC architectures, the hetero-CPI shows outstanding durability, with 86% and 92% of the original PCE preserved for n-i-p and p-i-n structures, respectively. As shown in the insets of Fig. S16, the pristine ETL/OIHP interface shows obvious delamination and pinholes after thermal cycling tests that is the result of its deficiency in interfacial mechanical properties. Homo- and hetero-CPI cases, in contrast, do not exhibit any obvious interfacial defects after being subjected to this same thermal cycling test. These results again demonstrate the benefits of the OIHP with CPI produces high mechanical integrity and tolerance. We further investigated the bending mechanical property of $(PEA)_2PbI_4$, $(R\text{-MBA})_2PbI_4$, and $(R/S\text{-MBA})_2PbI_4$ films on PEN/ITO substrate (**Fig. S17**). $(R/S\text{-MBA})_2PbI_4$ and $(R\text{-MBA})_2PbI_4$ films show strong resistance to crack generation after 100 times bending cycle, compared to $(PEA)_2PbI_4$ with obvious crack formation. This result implies that the chiral interface modulates ETL/OIHP and could resemble mechanical springiness with a larger toughness over the nonchiral interface.

As mentioned above, the role of chiral molecule enantiomers influences the molecular packing configurations within the heterointerface, affecting intermolecular interactions and structural stability. We have also tested other categories of R or S ammonium molecules, R-2-amino-1,1,1-trifluoropropane hydrochloride ($R\text{-CF}_3$) and *S*-2-amino-1,1,1-trifluoropropane hydrochloride ($S\text{-CF}_3$). Using this pair of chiral molecules, we also fabricated homo-chiral (homo-CF_3) or hetero-chiral (hetero-CF_3) interfaces between the OIHP and ETL in n-i-p structured PSCs. Based on the results of PV performance, stability, and mechanical properties, the PSCs based on hetero-CF_3 and homo-CF_3 consistently show advantages over pristine SnO_2, and the hetero-CF_3 shows a higher level of enhancement (**Fig. S18**). These results are consistent with the MBAI-based chiral interface modification, demonstrating the generality of the CPI approach.

Discussion

We have shown that chiral-structured perovskite interlayers with dynamically durable chiral packing enhance the mechanical, chemical, and carrier-extracting properties of the ETL/OIHP heterointerface. Highly efficient PSCs with chiral perovskite interlayers demonstrate promising tolerance to thermal cycling, damp heat, and light-soaking conditions. Furthermore, a heterochiral interlayer with a racemic mixture of right- and left-handedness shows additional enhancements, which harness the merits of the higher packing density of organic molecules, higher mixing entropy, and higher elastic modulus. The enhanced moisture stability for PSCs with hetero-CPI also benefits from strong in-plane binding and close hydrophobic benzene ring packing, thus preventing moisture from penetrating the interlayer between OIHP and ETL. These heterochiral findings have the potential to play a pivotal role in translating cell-level considerations to module-level stability assessments, marking a natural progression beyond existing research in this field. Our work presents a proof of principle for designing stable and efficient heterointerfaces by utilizing chiral perovskite interlayers with tailored chemical/physical/mechanical properties to further advance PSCs and other optoelectronic applications.

References and Notes:

1. R. Lin, Y. Wang, Q. Lu, B. Tang, J. Li, H. Gao, Y. Gao, H. Li, C. Ding, J. Wen, P. Wu, C. Liu, S. Zhao, K. Xiao, Z. Liu, C. Ma, Y. Deng, L. Li, F. Fan, H. Tan, All-perovskite tandem solar cells with 3D/3D bilayer perovskite heterojunction. *Nature* **620**, 994–1000 (2023).
2. E. Aydin, E. Ugur, B. K. Yildirim, T. G. Allen, P. Dally, A. Razzaq, F. Cao, L. Xu, B. Vishal, A. Yazmaciyan, A. A. Said, S. Zhumagali, R. Azmi, M. Babics, A. Fell, C. Xiao, S. De Wolf, Enhanced optoelectronic coupling for perovskite/silicon tandem solar cells. *Nature* **623**, 732–738 (2023).
3. C. Ma, F. T. Eickemeyer, S.-H. Lee, D.-H. Kang, S. J. Kwon, M. Grätzel, N.-G. Park, Unveiling facet-dependent degradation and facet engineering for stable perovskite solar cells. *Science* **379**, 173–178 (2023).
4. S. Yu, Z. Xiong, H. Zhou, Q. Zhang, Z. Wang, F. Ma, Z. Qu, Y. Zhao, X. Chu, X. Zhang, J. You, Homogenized NiO_x nanoparticles for improved hole transport in inverted perovskite solar cells. *Science* **382**, 1399–1404 (2023).
5. Z. Li, X. Sun, X. Zheng, B. Li, D. Gao, S. Zhang, X. Wu, S. Li, J. Gong, J. M. Luther, Z. Li, Z. Zhu, Stabilized hole-selective layer for high-performance inverted p-i-n perovskite solar cells. *Science* **382**, 284–289 (2023).
6. C. Liu, Y. Yang, H. Chen, J. Xu, A. Liu, A. S. R. Bati, H. Zhu, L. Grater, S. S. Hadke, C. Huang, V. K. Sangwan, T. Cai, D. Shin, L. X. Chen, M. C. Hersam, C. A. Mirkin, B. Chen, M. G. Kanatzidis, E. H. Sargent, Bimolecularly passivated interface enables efficient and stable inverted perovskite solar cells. *Science* **382**, 810–815 (2023).
7. J. Park, J. Kim, H.-S. Yun, M. J. Paik, E. Noh, H. J. Mun, M. G. Kim, T. J. Shin, S. I. Seok, Controlled growth of perovskite layers with volatile alkylammonium chlorides. *Nature*, 1–7 (2023).
8. J.-P. Correa-Baena, M. Saliba, T. Buonassisi, M. Grätzel, A. Abate, W. Tress, A. Hagfeldt, Promises and challenges of perovskite solar cells. *Science* **358**, 739–744 (2017).
9. Best Research-Cell Efficiency Chart. https://www.nrel.gov/pv/cell-efficiency.html.
10. Z. Dai, N. P. Padture, Challenges and opportunities for the mechanical reliability of metal halide perovskites and photovoltaics. *Nat. Energy* **8**, 1319–1327 (2023).
11. Y. Zhou, L. M. Herz, A. K.-Y. Jen, M. Saliba, Advances and challenges in understanding the microscopic structure–property–performance relationship in perovskite solar cells. *Nat. Energy* **7**, 794–807 (2022).
12. G. Li, Z. Su, L. Canil, D. Hughes, M. H. Aldamasy, J. Dagar, S. Trofimov, L. Wang, W. Zuo, J. J. Jerónimo-Rendon, M. M. Byranvand, C. Wang, R. Zhu, Z. Zhang, F. Yang, G. Nasti, B. Naydenov, W. C. Tsoi, Z. Li, X. Gao, Z. Wang, Y. Jia, E. Unger, M. Saliba, M. Li, A. Abate,

Highly efficient p-i-n perovskite solar cells that endure temperature variations. *Science* **379**, 399–403 (2023).

13. Z. Dai, S. K. Yadavalli, M. Chen, A. Abbaspourtamijani, Y. Qi, N. P. Padture, Interfacial toughening with self-assembled monolayers enhances perovskite solar cell reliability. *Science* **372**, 618–622 (2021).

14. N. Rolston, A. D. Printz, J. M. Tracy, H. C. Weerasinghe, D. Vak, L. J. Haur, A. Priyadarshi, N. Mathews, D. J. Slotcavage, M. D. McGehee, R. E. Kalan, K. Zielinski, R. L. Grimm, H. Tsai, W. Nie, A. D. Mohite, S. Gholipour, M. Saliba, M. Grätzel, R. H. Dauskardt, Effect of Cation Composition on the Mechanical Stability of Perovskite Solar Cells. *Adv. Energy Mater.* **8**, 1702116 (2018).

15. J. He, T. Li, X. Liu, H. Su, Z. Ku, J. Zhong, F. Huang, Y. Peng, Y.-B. Cheng, Influence of phase transition on stability of perovskite solar cells under thermal cycling conditions. *Solar Energy* **188**, 312–317 (2019).

16. G. Li, Z. Su, M. Li, H. K. H. Lee, R. Datt, D. Hughes, C. Wang, M. Flatken, H. Köbler, J. J. Jerónimo-Rendon, R. Roy, F. Yang, J. Pascual, Z. Li, W. C. Tsoi, X. Gao, Z. Wang, M. Saliba, A. Abate, Structure and Performance Evolution of Perovskite Solar Cells under Extreme Temperatures. *Adv. Energy Mater.* **12**, 2202887 (2022).

17. G. Yuan, W. Xie, Q. Song, S. Ma, Y. Ma, C. Shi, M. Xiao, F. Pei, X. Niu, Y. Zhang, J. Dou, C. Zhu, Y. Bai, Y. Wu, H. Wang, Q. Fan, Q. Chen, Inhibited Crack Development by Compressive Strain in Perovskite Solar Cells with Improved Mechanical Stability. *Adv. Mater.* **35**, 2211257 (2023).

18. H. Wang, C. Zhu, L. Liu, S. Ma, P. Liu, J. Wu, C. Shi, Q. Du, Y. Hao, S. Xiang, H. Chen, P. Chen, Y. Bai, H. Zhou, Y. Li, Q. Chen, Interfacial Residual Stress Relaxation in Perovskite Solar Cells with Improved Stability. *Adv. Mater.* **31**, 1904408 (2019).

19. R. Cheacharoen, C. C. Boyd, G. F. Burkhard, T. Leijtens, J. A. Raiford, K. A. Bush, S. F. Bent, M. D. McGehee, Encapsulating perovskite solar cells to withstand damp heat and thermal cycling. *Sustain. Energy Fuels.* **2**, 2398–2406 (2018).

20. S. Mariotti, E. Köhnen, F. Scheler, K. Sveinbjörnsson, L. Zimmermann, M. Piot, F. Yang, B. Li, J. Warby, A. Musiienko, D. Menzel, F. Lang, S. Keßler, I. Levine, D. Mantione, A. Al-Ashouri, M. S. Härtel, K. Xu, A. Cruz, J. Kurpiers, P. Wagner, H. Köbler, J. Li, A. Magomedov, D. Mecerreyes, E. Unger, A. Abate, M. Stolterfoht, B. Stannowski, R. Schlatmann, L. Korte, S. Albrecht, Interface engineering for high-performance, triple-halide perovskite–silicon tandem solar cells. *Science* **381**, 63–69 (2023).

21. S. Zhang, F. Ye, X. Wang, R. Chen, H. Zhang, L. Zhan, X. Jiang, Y. Li, X. Ji, S. Liu, M. Yu, F. Yu, Y. Zhang, R. Wu, Z. Liu, Z. Ning, D. Neher, L. Han, Y. Lin, H. Tian, W. Chen, M. Stolterfoht, L. Zhang, W.-H. Zhu, Y. Wu, Minimizing buried interfacial defects for efficient inverted perovskite solar cells. *Science* **380**, 404–409 (2023).

22. Q. Jiang, J. Tong, Y. Xian, R. A. Kerner, S. P. Dunfield, C. Xiao, R. A. Scheidt, D. Kuciauskas, X. Wang, M. P. Hautzinger, R. Tirawat, M. C. Beard, D. P. Fenning, J. J. Berry, B.

W. Larson, Y. Yan, K. Zhu, Surface reaction for efficient and stable inverted perovskite solar cells. *Nature* **611**, 278–283 (2022).

23. J. Crassous, M. J. Fuchter, D. E. Freedman, N. A. Kotov, J. Moon, M. C. Beard, S. Feldmann, Materials for chiral light control. *Nat. Rev. Mater.* **8**, 365–371 (2023).

24. Y.-H. Kim, Y. Zhai, H. Lu, X. Pan, C. Xiao, E. A. Gaulding, S. P. Harvey, J. J. Berry, Z. V. Vardeny, J. M. Luther, Chiral-induced spin selectivity enables a room-temperature spin light-emitting diode. *Science* **371**, 1129–1133 (2021).

25. G. K. Long, R. Sabatini, M. I. Saidaminov, G. Lakhwani, A. Rasmita, X. G. Liu, E. H. Sargent, W. B. Gao, Chiral-perovskite optoelectronics. *Nat. Rev. Mater.* **5**, 423–439 (2020).

26. M. K. Jana, R. Song, H. Liu, D. R. Khanal, S. M. Janke, R. Zhao, C. Liu, Z. Valy Vardeny, V. Blum, D. B. Mitzi, Organic-to-inorganic structural chirality transfer in a 2D hybrid perovskite and impact on Rashba-Dresselhaus spin-orbit coupling. *Nat. Commun.* **11**, 4699 (2020).

27. J. D. Watson, F. H. C. Crick, Molecular Structure of Nucleic Acids: A Structure for Deoxyribose Nucleic Acid. *Nature* **171**, 737–738 (1953).

28. I. Gutsche, A. Desfosses, G. Effantin, W. L. Ling, M. Haupt, R. W. H. Ruigrok, C. Sachse, G. Schoehn, Near-atomic cryo-EM structure of the helical measles virus nucleocapsid. *Science* **348**, 704–707 (2015).

29. B. D. Wilts, B. Apeleo Zubiri, M. A. Klatt, B. Butz, M. G. Fischer, S. T. Kelly, E. Spiecker, U. Steiner, G. E. Schröder-Turk, Butterfly gyroid nanostructures as a time-frozen glimpse of intracellular membrane development. *Sci. Adv.* **3**, e1603119 (2017).

30. V. Sharma, M. Crne, J. O. Park, M. Srinivasarao, Structural Origin of Circularly Polarized Iridescence in Jeweled Beetles. *Science* **325**, 449–451 (2009).

31. E. Babaev, D. Kharzeev, M. Larsson, A. Molochkov, V. Zhaunerchyk, *Chiral Matter* (WORLD SCIENTIFIC, 2023).

32. T. Frenzel, M. Kadic, M. Wegener, Three-dimensional mechanical metamaterials with a twist. *Science* **358**, 1072–1074 (2017).

33. W. Wu, D. Qi, H. Liao, G. Qian, L. Geng, Y. Niu, J. Liang, Deformation mechanism of innovative 3D chiral metamaterials. *Sci. Rep.* **8**, 12575 (2018).

34. X. Ning, X. Yu, H. Wang, R. Sun, R. E. Corman, H. Li, C. M. Lee, Y. Xue, A. Chempakasseril, Y. Yao, Z. Zhang, H. Luan, Z. Wang, W. Xia, X. Feng, R. H. Ewoldt, Y. Huang, Y. Zhang, J. A. Rogers, Mechanically active materials in three-dimensional mesostructures. *Sci. Adv.* **4**, eaat8313 (2018).

35. W. Wu, W. Hu, G. Qian, H. Liao, X. Xu, F. Berto, Mechanical design and multifunctional applications of chiral mechanical metamaterials: A review. *Mater. Des.* **180**, 107950 (2019).

36. A. M. Wahl, *Mechanical Springs* (McGraw-Hill, 1963).

37. L. Scalon, J. Brunner, M. G. D. Guaita, R. Szostak, M. Albaladejo-Siguan, T. Kodalle, L. A. Guerrero-León, C. M. Sutter-Fella, C. C. Oliveira, Y. Vaynzof, A. F. Nogueira, Tuning Phase Purity in Chiral 2D Perovskites. *Adv. Opt. Mater.* 2300776 (2023).

38. D. G. Billing, A. Lemmerer, Synthesis and crystal structures of inorganic–organic hybrids incorporating an aromatic amine with a chiral functional group. *Crystengcomm* **8**, 686–695 (2006).

39. D. G. Billing, Bis(1-phenyl-ethyl-ammonium) tetra-iodo-plumbate(II). *Acta Cryst. E* **58**, m669–m671 (2002).
40. J. Peng, G. J. Snyder, A figure of merit for flexibility. *Science* **366**, 690–691 (2019).
41. T. Li, C. Chen, A. H. Brozena, J. Y. Zhu, L. Xu, C. Driemeier, J. Dai, O. J. Rojas, A. Isogai, L. Wågberg, L. Hu, Developing fibrillated cellulose as a sustainable technological material. *Nature* **590**, 47–56 (2021).
42. B. S. Lazarus, C. Chadha, A. Velasco-Hogan, J. D. V. Barbosa, I. Jasiuk, M. A. Meyers, Engineering with keratin: A functional material and a source of bioinspiration. *iScience* **24**, 102798 (2021).
43. G. Tang, C. Yang, A. Stroppa, D. Fang, J. Hong, Revealing the role of thiocyanate anion in layered hybrid halide perovskite $(CH_3NH_3)_2Pb(SCN)_2I_2$. *J. Chem. Phys.* **146**, 224702 (2017).
44. D. L. McGott, C. P. Muzzillo, C. L. Perkins, J. J. Berry, K. Zhu, J. N. Duenow, E. Colegrove, C. A. Wolden, M. O. Reese, 3D/2D passivation as a secret to success for polycrystalline thin-film solar cells. *Joule* **5**, 1057–1073 (2021).
45. D. W. de Quilettes, S. M. Vorpahl, S. D. Stranks, H. Nagaoka, G. E. Eperon, M. E. Ziffer, H. J. Snaith, D. S. Ginger, Impact of microstructure on local carrier lifetime in perovskite solar cells. *Science* **348**, 683–686 (2015).
46. M. J. Trimpl, A. D. Wright, K. Schutt, L. R. V. Buizza, Z. Wang, M. B. Johnston, H. J. Snaith, P. Müller-Buschbaum, L. M. Herz, Charge-Carrier Trapping and Radiative Recombination in Metal Halide Perovskite Semiconductors. *Adv. Funct. Mater.* **30**, 2004312 (2020).
47. D. W. deQuilettes, S. Jariwala, S. Burke, M. E. Ziffer, J. T.-W. Wang, H. J. Snaith, D. S. Ginger, Tracking Photoexcited Carriers in Hybrid Perovskite Semiconductors: Trap-Dominated Spatial Heterogeneity and Diffusion. *ACS Nano* **11**, 11488–11496 (2017).
48. Y. Yang, B. Rice, X. Shi, J. R. Brandt, R. Correa da Costa, G. J. Hedley, D.-M. Smilgies, J. M. Frost, Ifor. D. W. Samuel, A. Otero-de-la-Roza, E. R. Johnson, K. E. Jelfs, J. Nelson, A. J. Campbell, M. J. Fuchter, Emergent Properties of an Organic Semiconductor Driven by its Molecular Chirality. *ACS Nano* **11**, 8329–8338 (2017).
49. M. Chen, X. Jiao, J. Li, W. Wu, H. Xin, C. R. McNeill, X. Gao, From Homochiral Assembly to Heterochiral Assembly: A Leap in Charge Transport Properties of Binaphthol-Based Axially Chiral Materials. *Langmuir* **35**, 6188–6195 (2019).

Acknowledgments

Funding: Y.Z. acknowledges the Early Career Scheme (No. 22300221), General Research Fund (No. 12302822) from the Hong Kong Research Grant Council (RGC). This work was authored in part by the National Renewable Energy Laboratory, operated by Alliance for Sustainable Energy, LLC, for the U.S. Department of Energy (DOE) under Contract No. DE-AC36-08GO28308. K.Z., J.M.L., and J.J.B. acknowledge the support on chiral interlayer studies from the Center for Hybrid Organic-Inorganic Semiconductors for Energy (CHOISE), an Energy Frontier Research Center funded by the Office of Basic Energy Sciences, Office of Science within the U.S. Department of Energy. S.Y. and M.C. acknowledge the support on device fabrication and stability studies from the Advanced Perovskite Cells and Modules program, funded by the U.S. Department of Energy, Office of Energy Efficiency and Renewable Energy, Solar Energy Technologies Office Award Number 38256. P.G. acknowledges the support from the National Science Foundation (NSF) under Grant No. DMR-2313648. The work at Yale University was supported by the U.S. National Science Foundation (Grant No. CHE-2305138). T.D. acknowledges the RGC Postdoctoral Fellowship Scheme. We also acknowledge the experimental assistance provided by M. Hao, C. Yang, Dr. T. Liu, O. Durak, and DFT calculation by Dr. X. Zhang from ΣLAB, Dr. Z. Ma for her contribution to the measurement of mechanical properties, and Dr. S. Guo from the Hong Kong Polytechnic University for conducting the cross-sectional SEM measurements. Additionally, we extend our gratitude to Dr. Laura Schelhas for her constructive comments. The U.S. Government retains and the publisher, by accepting the article for publication, acknowledges that the U.S. Government retains a nonexclusive, paid-up, irrevocable, worldwide license to publish or reproduce the published form of this work, or allow others to do so, for U.S. Government purposes.

Author contributions: Y.Z. conceived the idea and directed the project. Y.Z. and T.D. co-designed the experiments. T.D. performed the sample preparation, device fabrication and testing, materials characterization (scanning electron microscopy, atomic force microscopy, X-ray diffraction, UV-vis, etc.), and delamination experiments. S.Y. optimized the device fabrication under the supervision of K.Z. M.C. performed thermal-cycling stability tests under the supervision of J.M.L. W.Y. assisted with the device fabrication and testing. P.G. and L.Y. performed the photoluminescence experiments. J.J.B., J.ML., and K.Z. contributed to analyzing the materials and device mechanisms. T.D. and Y.Z. drafted the manuscript with inputs from all co-authors. **Competing interests:** Authors declare no competing interests. **Data and materials availability:** All data is available in the main text or the supplementary materials.

Supplementary Materials

Materials and Methods

Figs S1 to S18

Tables S1 to S5